J Solid State Electrochem (2012) 16:135–142
DOI 10.1007/s10008-011-1306-y

ORIGINAL PAPER

Synthesis and characterization of mesoporous Mn–Ni oxides for supercapacitors

Dao-Lai Fang · Bing-Cai Wu · Yong Yan · Ai-Qin Mao · Cui-Hong Zheng

Received: 10 November 2010 / Revised: 31 December 2010 / Accepted: 7 January 2011 / Published online: 25 January 2011

Abstract Mesoporous Mn–Ni oxides with the chemical compositions of $Mn_{1-x}Ni_xO_\delta$ (x=0, 0.2, and 0.4) were prepared by a solid-state reaction route, using manganese sulfate, nickel chloride, and potassium hydroxide as starting materials. The obtained Mn–Ni oxides, mainly consisting of the phases of α- and γ-MnO_2, presented irregular mesoporous agglomerates built from ultra-fine particles. Specific surface area of $Mn_{1-x}Ni_xO_\delta$ was 42.8, 59.6, and 84.5 $m^2\ g^{-1}$ for x=0, 0.2, and 0.4, respectively. Electrochemical properties were investigated by cyclic voltammetry and galvanostatic charge/discharge in 6 mol L^{-1} KOH electrolyte. Specific capacitances of $Mn_{1-x}Ni_xO_\delta$ were 343, 528, and 411 F g^{-1} at a scan rate of 2 mV s^{-1} for x=0, 0.2, and 0.4, respectively, and decreased to 157, 183, and 130 F g^{-1} with increasing scan rate to 100 mV s^{-1}, respectively. After 500 cycles at a current density of 1.24 A g^{-1}, the symmetrical $Mn_{1-x}Ni_xO_\delta$ capacitors delivered specific capacitances of 160, 250, and 132 F g^{-1} for x=0, 0.2, and 0.4, respectively, retaining about 82%, 89%, and 75% of their respective initial capacitances. The $Mn_{0.8}Ni_{0.2}O_\delta$ material showed better supercapacitive performance, which was promising for supercapacitor applications.

Keywords Supercapacitors · Mn–Ni oxides · Solid-state reaction · Cyclic voltammetry · Capacitive performance

D.-L. Fang (✉) · B.-C. Wu · Y. Yan · A.-Q. Mao · C.-H. Zheng
School of Materials Science and Engineering and Anhui Key Laboratory of Metal Materials and Processing,
Anhui University of Technology,
Ma'anshan, Anhui 243002, People's Republic of China
e-mail: fangdl@ustc.edu

Introduction

Electrochemical capacitors, often called supercapacitors, show the unique energy-storage performance, i.e. larger power density and longer life cycle when compared with secondary batteries, and higher energy density when compared with conventional capacitors [1]. Therefore, supercapacitors have great potential in various fields, such as hybrid power sources, peak power sources, backup power storage, lightweight electronic fuses, and starting power of fuel cells [2, 3]. Based on their charge-storage mechanism, supercapacitors can be classified into two categories: (a) electrical double-layer capacitors, which are based on the double-layer capacitance arising from the nonfaradic charge separation at an electrode/electrolyte interface, mainly focusing on carbon materials [4, 5]; (b) pseudocapacitors, which store energy by the pseudocapacitance originating from fast and reversible faradic redox reactions of electroactive materials, mainly focusing on transition metal oxides [6–9] and conducting polymers [10, 11].

For obtaining high energy density supercapacitors, researchers have devoted great efforts to search for excellent pseudocapacitive materials [12–21]. Amorphous hydrated ruthenium oxide has been demonstrated to be an ideal pseudocapacitive material, owing to its high conductivity, good electrochemical stability, and large specific capacitance (SC) of 720–760 F g^{-1} [12]. However, high cost and toxicity of the ruthenium oxide limit its commercial applications. Thus, the less expensive and less toxic alternatives, such as amorphous MnO_2 [13, 14], nanostructured NiO [15, 16], and mesoporous and nanowire-array Co_3O_4 [17, 18], have been developed as electrode materials for supercapacitors. Also, crystallized MnO_2 with a two-dimensional birnessite structure has

been revealed to have an advantage of obtaining a relatively high capacitance despite its moderate specific surface area [19, 20]. These transition metal oxides exhibit remarkable capacitive nature, delivering a considerable specific capacitance. Unfortunately, these pristine transition metal oxides are less electrically conductive, which causes a large equivalent series resistance for electrodes fabricated from these materials. As a result, the maximum capacity and power density available for the electrodes are greatly limited. Recently, it has been demonstrated that incorporation of Ni [21], Mo [22], V [23], Pb [24], and Co [25, 26] into manganese oxide can remarkably improve its capacitive performance. Nevertheless, to the best of our knowledge, Mn–Ni oxides as electrode materials for supercapacitors have not been fully investigated yet [8, 21] and how the doped nickel content affects their electrochemical properties is still ambiguous.

In this work, mesoporous Mn–Ni oxides with the chemical compositions of $Mn_{1-x}Ni_xO_\delta$ (x=0, 0.2, and 0.4) were prepared by a solid-state reaction route, i.e. milling a mixture of the starting materials of manganese sulfate, nickel chloride, and potassium hydroxide, followed by washing, filtrating, and calcining the milled mixture. The Mn–Ni oxides were characterized by the techniques of X-ray diffraction (XRD), scanning electron microscope (SEM), nitrogen adsorption–desorption measurements, cyclic voltammetry, and galvanostatic charge/discharge cycling. Considering the considerable content of nickel added in the prepared Mn–Ni oxides, and a remarkable pseudocapacitive behavior of nickel oxide in alkaline aqueous electrolyte [15, 16, 27, 28], KOH aqueous electrolyte was used to investigate the electrochemical properties of the Mn–Ni oxides. The obtained $Mn_{0.8}Ni_{0.2}O_\delta$ electrode shows excellent capacitive performance in terms of SC, power capability, and cycling stability. The $Mn_{0.8}Ni_{0.2}O_\delta$ material has great potential for supercapacitors.

Experimental

Synthesis of the ultra-fine Mn–Ni oxides

Analytical-grade manganese sulfate $MnSO_4{\cdot}H_2O$, nickel chloride $NiCl_2{\cdot}6H_2O$, and potassium hydroxide KOH were used as starting materials. All the reagents were purchased from Sinopharm Group Chemical Reagent Company in China, and used as received. For synthesis of the Mn–Ni oxides with the expected chemical compositions of $Mn_{1-x}Ni_xO_\delta$ (x=0, 0.2, and 0.4), a proper amount of the starting materials was weighed accurately with a molar ratio of $MnSO_4{\cdot}H_2O/NiCl_2{\cdot}6H_2O$/KOH of (1-$x$): x: 2, then mixed and milled in a mortar to form a powder mixture. In a typical procedure, 0.04 mol of $MnSO_4{\cdot}H_2O$ (6.7604 g), 0.01 mol of $NiCl_2{\cdot}6H_2O$ (2.3769 g) and 0.10 mol of KOH (5.6110 g) were used for obtaining 0.05 mol of the Mn–Ni oxide of $Mn_{0.8}Ni_{0.2}O_\delta$. Subsequently, the obtained powder mixture was ball milled at room temperature for 5 h in a polyethylene container using zirconia balls as milling medium. The milled mixture was fully washed and filtrated with de-ionized water, then dried at 80 °C. Finally, the dried mixture was calcined in air at 350 °C for 10 h.

Structural characterization

A Philips X'pert Pro X-ray diffractometer with Cu K_α radiation (λ=1.5406 Å) was used to analyze the phase compositions of the prepared Mn–Ni oxides. Diffraction data were collected in the 2θ range from 20° to 80°, using the step-scan mode with a scanning speed of 0.02° step-size and 1 s per step. The morphologies of the obtained Mn–Ni oxides were observed by using a JSM 6490 SEM.

The chemical compositions of the Mn–Ni oxides were determined by inductively coupled plasma-atomic emission spectroscopy (ICP-AES) on a Model Atomscan Advantage spectrometer (Thermo Jarrell Ash Co., USA). Samples of the Mn–Ni oxides were digested for 3 h at 65 °C in concentrated hydrochloric acid with a small amount of hydrogen peroxide H_2O_2 added, and then the obtained solutions were further diluted for determination of the Mn and Ni contents. Its relative standard deviation is less than 1%.

Nitrogen adsorption–desorption measurements were carried out at a Coulter SA 3100 system at 77.3 K. The surface area was calculated using the Brunauer–Emmett–Teller (BET) equation. Pore-size distributions were calculated by the Barrett–Joyner–Halenda (BJH) method. Samples were dried and degassed for 2 h at 150 °C to remove any surface organic or moisture contaminants.

The electrodes for electrochemical measurements consisted of the electroactive materials of the prepared Mn–Ni oxides, acetylene black, and polytetrafluoroethylene (PTFE), whose weight ratio was 75:20:5. Firstly, the Mn–Ni oxides and the acetylene black were fully mixed and ground, then a proper amount of PTFE binder was added into the powder mixture to achieve a homogeneous slurry, followed by painting the prepared slurry onto a nickel foam current collector with an area of 1×1.5 cm. Finally, the painted current collector was dried for 10 h at 80 °C, and pressed at a pressure of 10 MPa to form a reliable electrode with the thickness of ~120 μm. The mass of the composite electrode fabricated is ~7 mg, including ~5.3 mg of the electroactive material.

All the electrochemical measurements concerned were carried out in 6 mol L^{-1} KOH aqueous electrolyte. Cyclic voltammetric measurements were performed on a CHI604C electrochemical workstation in a three-electrode cell set-up, using a Mn–Ni oxide electrode fabricated as the working electrode, a platinum foil as the counter electrode, a saturated calomel electrode (SCE) as the reference electrode. Cyclic voltammograms (CVs) at various scan rates were recorded between −0.4 and 0.4 V vs. SCE.

For evaluation of galvanostatic charge/discharge performance of the fabricated Mn–Ni oxide electrodes, a symmetrical capacitor was assembled using a couple of the identical electrodes separated by a porous polypropylene separator. The galvanostatic charge/discharge performance at various current densities was determined by a battery test system of Neware BTS-3008 W in a potential range from 0 to 0.8 V.

Results and discussion

Phase compositions and microstructures of the as-prepared Mn–Ni oxides

The light-pink mixture of the starting materials rapidly turned light brown, and simultaneously a lot of aqueous vapor was given off, soon after it had been milled, indicating the occurrence of solid-state reactions. After ball milling for 5 h, a brown powder substance was formed, which was then fully washed and filtrated, finally calcined at 350 °C in air for 10 h, yielding a fine brown Mn–Ni oxide powder.

The chemical compositions of the obtained Mn–Ni oxides of $Mn_{1-x}Ni_xO_\delta$ (x=0.2, and 0.4) were analyzed by ICP-AES. The molar ratio of Mn to Ni ions in the Mn–Ni oxides was determined to be 0.793: 0.207 for the $Mn_{0.8}Ni_{0.2}O_\delta$ and 0.596: 0.404 for the $Mn_{0.6}Ni_{0.4}O_\delta$. The ICP-AES result shows that the actual compositions of the Mn–Ni oxides are very close to the expected ones. In principle, the solid-state reaction route should cause no appreciable deviation in the chemical compositions of the obtained Mn–Ni oxides [29]. In a sense, the stoichiometries of the obtained Mn–Ni oxides only depend on the purity of the starting materials used.

Figure 1 gives the XRD patterns of the as-prepared Mn–Ni oxides. Low intensity and broadening of the peaks in Fig. 1(a–c) indicate that the obtained Mn–Ni oxides are poorly crystallized, and/or that crystallites in the oxides are very fine. Furthermore, the diffraction peaks in Fig. 1(b and c) are broadened more notably, in comparison with those in Fig. 1(a). This suggests that the process of crystallization and growth of crystallites in the obtained $Mn_{0.8}Ni_{0.2}O_\delta$ and $Mn_{0.6}Ni_{0.4}O_\delta$ was restrained to a certain degree due to doped nickel.

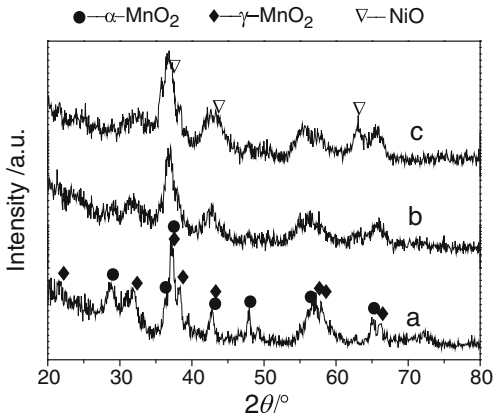

Fig. 1 XRD patterns of the as-prepared Mn–Ni oxides of (**a**) MnO_δ, (**b**) $Mn_{0.8}Ni_{0.2}O_\delta$, and (**c**) $Mn_{0.6}Ni_{0.4}O_\delta$

As shown in Fig. 1(a), the diffraction peaks at 2θ=28.8°, 37.2°, 42.1°, 47.9°, 56.3°, and 65.1° well match those of α-MnO_2 (JCPDS no. 44-0141), while the peaks at 2θ=21.8°, 32.2°, 37.1°, 38.4°, 42.6°, 56.7°, and 66.1° are in agreement with those of γ-MnO_2 (JCPDS no. 14-0644). This confirms that the prepared MnO_δ is mainly composed of a mixture of α- and γ-MnO_2, which is coincident with the XRD result of pristine manganese oxide synthesized in our previous work [30]. Due to lower intensity and serious broadening of the diffraction peaks in Fig. 1(b and c), it is a bit difficult to determine the phase compositions of the $Mn_{0.8}Ni_{0.2}O_\delta$ and $Mn_{0.6}Ni_{0.4}O_\delta$. Nevertheless, in comparison with the XRD pattern in Fig. 1(a), it is still clear that the XRD patterns in Fig. 1(b and c) actually contain almost all the diffraction peaks in Fig. 1(a), except for the small difference in the relative intensity of these peaks. This suggests that the α- and γ-MnO_2 phases formed in the MnO_δ are also contained in the $Mn_{0.8}Ni_{0.2}O_\delta$ and $Mn_{0.6}Ni_{0.4}O_\delta$. Clearly, no characteristic diffraction peaks for NiO (JCPDS no. 47-1049) can be observed in the XRD pattern in Fig. 1(b), indicating that no nickel oxide is detected in the $Mn_{0.8}Ni_{0.2}O_\delta$. This implies that most of the doped nickel ions may enter the crystal lattices of the α- and/or γ-MnO_2. Thus, it can be confirmed that the $Mn_{0.8}Ni_{0.2}O_\delta$ is mainly composed of the Ni-incorporated α- and γ-MnO_2 phases. However, the characteristic peaks for NiO (JCPDS no. 47-1049) can be obviously discerned in the XRD pattern in Fig. 1(c), revealing that not all of the doped Ni cations have been incorporated into the crystal lattices of α- and γ-MnO_2. This confirms that the prepared $Mn_{0.6}Ni_{0.4}O_\delta$ mainly consists of the Ni-incorporated α- and γ-MnO_2 phases, as well as a certain amount of poorly crystallized NiO.

Figure 2 shows the SEM images of the as-prepared Mn–Ni oxides. As seen from the SEM images in Fig. 2, the obtained Mn–Ni oxides consist of ultra-fine primary particles, which coalesce to form irregular porous agglomerates. Moreover, with increasing nickel content, the size of

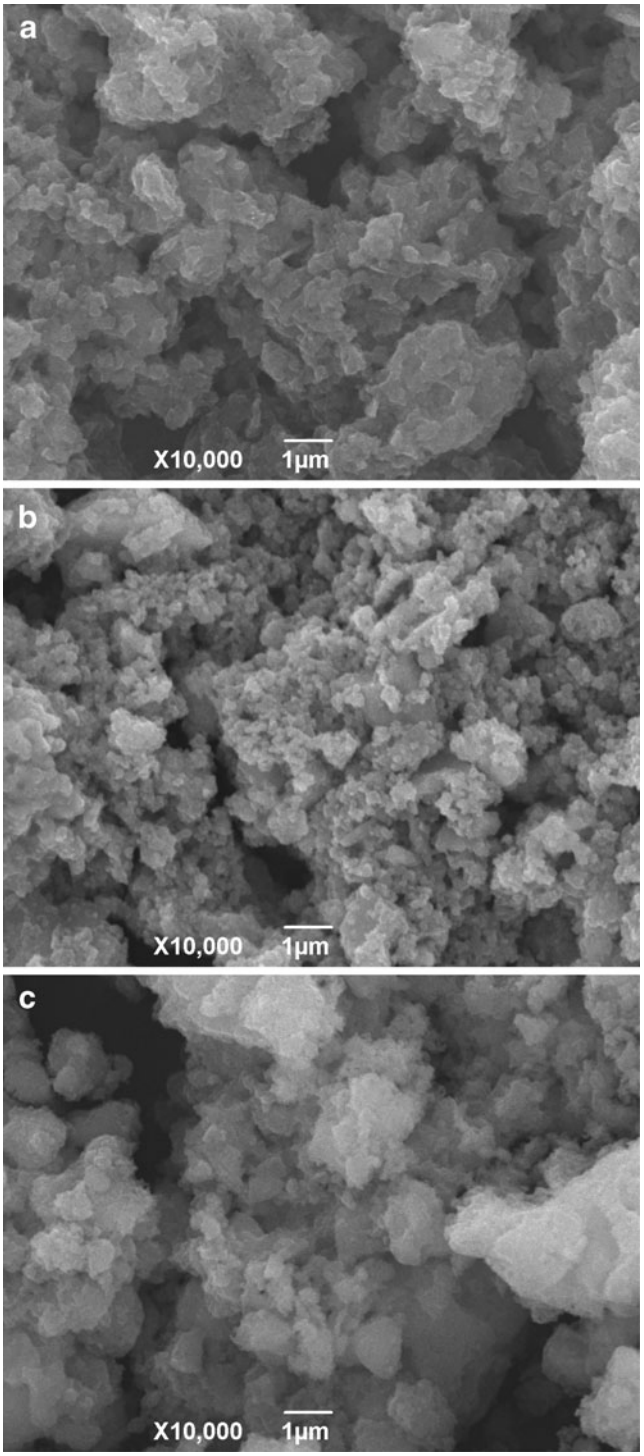

Fig. 2 SEM images of the as-prepared Mn–Ni oxides of (**a**) MnO_{δ}, (**b**) $Mn_{0.8}Ni_{0.2}O_{\delta}$, and (**c**) $Mn_{0.6}Ni_{0.4}O_{\delta}$

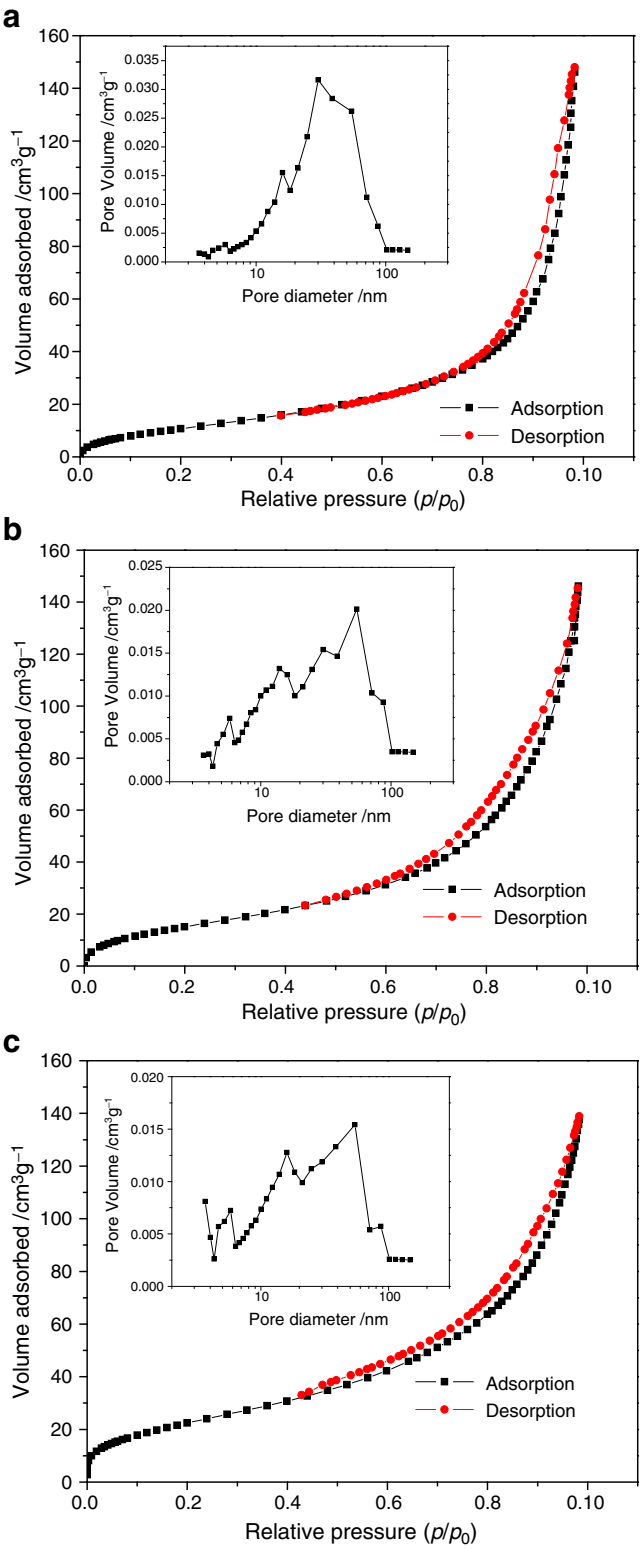

Fig. 3 N_2 adsorption–desorption isotherms and BJH pore-size distribution of the as-prepared Mn–Ni oxides of (**a**) MnO_{δ}, (**b**) $Mn_{0.8}Ni_{0.2}O_{\delta}$, and (**c**) $Mn_{0.6}Ni_{0.4}O_{\delta}$

the primary particles in the Mn–Ni oxides is increasingly fine, about 200 nm for the MnO_{δ}, and less than 100 nm for the $Mn_{0.6}Ni_{0.4}O_{\delta}$. This is in agreement with the XRD result in Fig. 1. Significantly, as electrode materials, the Mn–Ni oxides derived from the solid-state reaction route present a desired porous texture, which certainly makes it more

Table 1 Textural properties of the prepared Mn–Ni oxides from N_2 adsorption–desorption measurements

Samples	BET surface ($m^2\ g^{-1}$)	Pore volume ($cm^3\ g^{-1}$)	Average pore size (nm)
MnO_δ	42.76	0.2391	32.72
$Mn_{0.8}Ni_{0.2}O_\delta$	59.64	0.2374	30.49
$Mn_{0.6}Ni_{0.4}O_\delta$	84.47	0.2067	26.92

convenient for electroactive ions to diffuse and migrate between electrolyte and the electroactive oxides.

N_2 adsorption–desorption measurement at liquid N_2 temperature was used to investigate mesoporosity and textural properties of the as-prepared Mn–Ni oxides. Figure 3 gives the N_2 adsorption–desorption isotherms and BJH pore-size distribution of the Mn–Ni oxides. It can be seen that all the isotherms present a typical type IV sorption behavior, indicating a mesoporous structure of the Mn–Ni oxides according to the classification of IUPAC [31]. All the isotherms show an abrupt increase in adsorption volume of adsorbed N_2 at a certain P/P_0 value, which is about 0.67, 0.52, and 0.48 in Fig. 3(a–c), respectively. The sharp increase is generally due to capillary condensation, and the P/P_0 position of the inflection is related to the pore-size [32]. As revealed by the BJH pore-size distribution in the inset of Fig. 3, the pore-size distribution for the Mn–Ni oxides is almost situated in the mesoporous region (2–50 nm), indicating the desired microstructures of the $Mn_{1-x}Ni_xO_\delta$ oxides prepared by the solid-state reaction route. Detailed analyses disclose that the pore-size distribution increasingly shifts to the small-size range with increasing nickel content in the Mn–Ni oxides. For example, the volume percent of the pores with a diameter under 6 nm is about 4.69%, 10.65%, and 13.33% for the samples of MnO_δ, $Mn_{0.8}Ni_{0.2}O_\delta$ and $Mn_{0.6}Ni_{0.4}O_\delta$, respectively. Also the textural properties of the Mn–Ni oxides are given in Table 1. As shown in the Table 1, the BET surface area of the Mn–Ni oxides increases monotonously with increasing nickel content, while the average pore size and the pore volume decrease monotonously. This can be well explained by the XRD and SEM results, which indicate that the Mn–Ni oxides with higher nickel content are built from finer primary particles.

Electrochemical properties of the obtained Mn–Ni oxides

Cyclic voltammetry is considered to be a powerful tool to indicate capacitive behavior of electrode materials. In our previous work [30], it has been demonstrated that a potential range from −0.4 to 0.4 V vs. SCE is proper for pristine MnO_2 in KOH aqueous electrolyte. Also pristine NiO exhibits a significant pseudocapacitive behavior in KOH aqueous electrolyte in a potential range from 0 to 0.4 V vs. SCE [33]. Thus, the potential window between −0.4 and 0.4 V vs. SCE was set for the prepared Mn–Ni oxides in KOH aqueous electrolyte. Figure 4 shows the CVs of the Mn–Ni oxide electrodes at a scan rate of 5 mV s^{-1} in 6 mol L^{-1} KOH electrolyte. Clearly, the positive sweeps of all the CVs are roughly symmetric to their corresponding negative sweeps, suggesting the good electrochemical reversibility of the Mn–Ni oxide electrodes. Moreover, a couple of distinct redox peaks are observed in the potential range from 0.1 to 0.4 V vs. SCE, indicating the remarkable pseudocapacitive behavior of the prepared Mn–Ni oxides. It is generally accepted that in KOH aqueous electrolyte, the charge–discharge process in manganese oxide involves the fast quasi-reversible redox reaction based on the so-called proton–electron mechanism [34, 35]:

$$MnO_x(OH)_y + \delta H^+ + \delta e^- \rightleftarrows MnO_{x-\delta}(OH)_{y+\delta} \quad (1)$$

where $MnO_x(OH)_y$ and $MnO_{x-\delta}(OH)_{y+\delta}$ represent the interficial oxymanganese species under higher and lower oxidation states, respectively. The charge–discharge mechanism of nickel oxide in KOH aqueous electrolyte has been expressed as the electrochemical redox reaction [27, 28]:

$$NiO + OH^- \rightleftarrows NiOOH + e^- \quad (2)$$

As shown in Fig. 4(a), the anodic peak P1 at ~0.39 V is due to the oxidation of $MnO_{x-\delta}(OH)_{y+\delta}$ to $MnO_x(OH)_y$, while the cathodic peak P2 at ~0.27 V is for the reverse

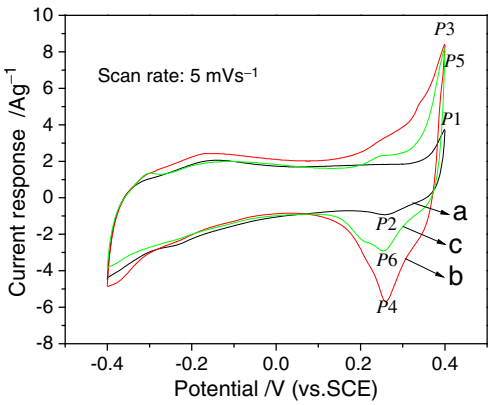

Fig. 4 Cyclic voltammograms (CVs) of the Mn–Ni oxide electrodes of (**a**) MnO_δ, (**b**) $Mn_{0.8}Ni_{0.2}O_\delta$, and (**c**) $Mn_{0.6}Ni_{0.4}O_\delta$ at a scan rate of 5 mV s^{-1}, using an aqueous solution of 6 mol L^{-1} KOH as the electrolyte, and a saturated calomel electrode as the reference electrode

process. The anodic peaks of P3 and P5 at ~0.38 V and the cathodic ones of P4 and P6 at ~0.25 V, as indicated in Fig. 4(b and c), are attributed to the overlapping of the electrochemical redox reactions of manganese oxide and nickel oxide, which are described in the Eqs. 1 and 2, respectively. The roughly symmetric CVs in anodic and cathodic directions, as well as the small potential difference between the anodic and cathodic peaks, ranging from 0.10 to 0.12 V, indicate the good reversibility of the Mn–Ni oxide electrodes.

Importantly, the CV for the $Mn_{0.8}Ni_{0.2}O_{\delta}$ electrode shows larger current response of the redox peaks in the potential range of 0.1–0.4 V vs. SCE, in comparison with the ones for the MnO_{δ} and $Mn_{0.6}Ni_{0.4}O_{\delta}$ electrodes. This may be due to the difference in the phase compositions and microstructures of the prepared Mn–Ni oxides. As speculated from the aforementioned XRD result in Fig. 1 (b), most of the nickel cations in the $Mn_{0.8}Ni_{0.2}O_{\delta}$ may enter and occupy the lattices of α- and γ-MnO_2, which causes the seriously distorted lattices of the manganese oxide, allowing the $Mn_{0.8}Ni_{0.2}O_{\delta}$ a higher electrochemical activity. Moreover, as indicated by the result of N_2 adsorption–desorption measurements in Fig. 3, the $Mn_{0.8}Ni_{0.2}O_{\delta}$ contains lower volume percentage of micropores than the $Mn_{0.6}Ni_{0.4}O_{\delta}$, suggesting that a larger surface area is available for the electrochemical reactions in the $Mn_{0.8}Ni_{0.2}O_{\delta}$, despite its smaller BET surface area determined.

SC values of the Mn–Ni oxide electrodes were calculated from the CVs according to the formula $C_s = \frac{I}{m\upsilon}$, where C_s is the SC (F g^{-1}), m the mass (g) of the electroactive material, υ the potential scan rate (V s^{-1}), and I the even current response (A) defined by $I = \frac{1}{2(V_c - V_a)} \oint i dV$ (V_a and V_c represent the lowest and highest potentials (V), respectively). Figure 5(i) gives scan rate dependence of the SC values for the Mn–Ni oxide electrodes. SC values for the MnO_{δ}, $Mn_{0.8}Ni_{0.2}O_{\delta}$ and $Mn_{0.6}Ni_{0.4}O_{\delta}$ electrodes are 343, 528, and 411 F g^{-1} at a scan rate of 2 mV s^{-1}, respectively, and decrease to 157, 183, and 130 F g^{-1} with increasing scan rate to 100 mV s^{-1}, respectively. This indicates a larger SC of the $Mn_{0.8}Ni_{0.2}O_{\delta}$ electrode in a scan range of 2–100 mV s^{-1}, compared with the MnO_{δ} and $Mn_{0.6}Ni_{0.4}O_{\delta}$ electrodes. Importantly, a considerable SC value of 183 F g^{-1} is obtained at a high scan rate of 100 mV s^{-1}, indicating a higher power density of the $Mn_{0.8}Ni_{0.2}O_{\delta}$ electrode. Figure 5(ii) shows scan rate dependence of the current response for the Mn–Ni oxide electrodes. The apparently non-linear relation between current response and scan rate can be seen in Fig. 5(ii–*a* and *c*), which indicates the lower power property of the MnO_{δ} and $Mn_{0.6}Ni_{0.4}O_{\delta}$ electrodes. However, as shown in Fig. 5(ii—*b*), current response increases roughly linearly with increasing scan rate,

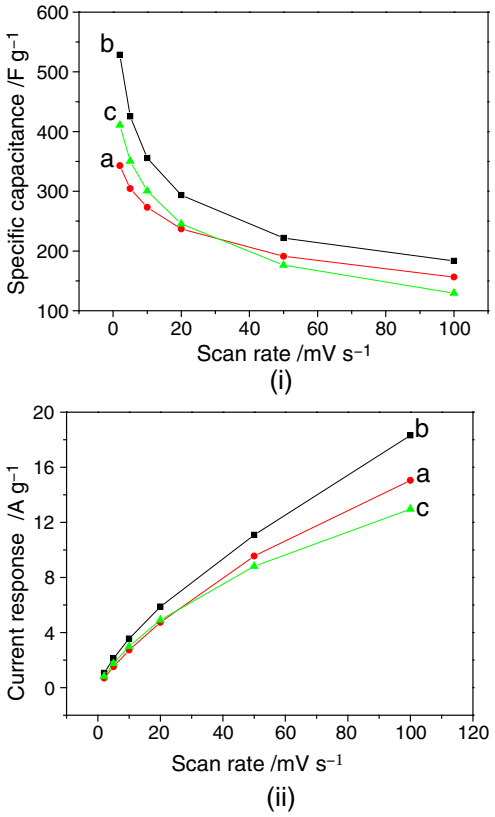

Fig. 5 Scan rate dependence of *i* SC values and *ii* current response for the Mn–Ni oxide electrodes of (**a**) MnO_{δ}, (**b**) $Mn_{0.8}Ni_{0.2}O_{\delta}$, and (**c**) $Mn_{0.6}Ni_{0.4}O_{\delta}$, using an aqueous solution of 6 mol L^{-1} KOH as the electrolyte, and a saturated calomel electrode as the reference electrode

confirming the higher power property of the $Mn_{0.8}Ni_{0.2}O_{\delta}$ electrode. Larger SC and higher power characteristic of the $Mn_{0.8}Ni_{0.2}O_{\delta}$ material could be ascribed to its unique chemical/phase compositions and microstructures. As elaborated in the above section of phase compositions and microstructures, the $Mn_{0.8}Ni_{0.2}O_{\delta}$ material is composed of the highly electroactive Ni-incorporated α- and γ-MnO_2 with a favorable mesoporous texture. In comparison with the pristine manganese oxide of α- and γ-MnO_2 derived from manganese oxalate in our previous work [30], the prepared $Mn_{0.8}Ni_{0.2}O_{\delta}$ shows the improved capacitive performance in terms of the SC and power property. Furthermore, compared with the pristine manganese oxide derived from other routes, such as sol–gel route [14], coprecipitation [36], and improved reduction reaction [37], the obtained $Mn_{0.8}Ni_{0.2}O_{\delta}$ material exhibits larger SC and higher power property. The facility and low cost of the present method of synthesis are highly advantageous from a commercial and economical point of view.

Symmetrical capacitors were assembled using a couple of the identical Mn–Ni oxide electrodes, and galvanostatic charge/discharge measurements were carried out in

6 mol L^{-1} KOH electrolyte in a potential range of 0–0.8 V. Figure 6 shows the galvanostatic charge/discharge profiles for the Mn–Ni oxide capacitors at different current densities. As illustrated in Fig. 6(a–c), during charging and discharging steps, the charge profile is nearly symmetric to its corresponding discharge counterpart with a slight curvature, indicating a remarkable pseudocapacitive characteristic of the Mn–Ni oxide materials. This is in accordance with the CVs in Fig. 4, where the strong redox peaks can be observed. SC of a symmetrical capacitor, expressed as SC of a single electrode, can be obtained by the formula of $C_s = \frac{4I\Delta t}{m\Delta V}$, where C_s is the discharge SC (F g^{-1}), I the discharge current (A), Δt the discharge time (s), m the total mass (g) of the electroactive material contained in the symmetrical capacitor, ΔV the discharge potential range (V) [33]. As given in Fig. 7(a–c), the SC values decrease with increasing discharging current density, being 313, 405, and 326 F g^{-1} at a current density of 0.155 A g^{-1} for the symmetrical MnO_δ, $Mn_{0.8}Ni_{0.2}O_\delta$, and $Mn_{0.6}Ni_{0.4}O_\delta$ capacitors, respectively. When increasing discharging current density to 1.24 A g^{-1}, the SC values for the symmetrical MnO_δ, $Mn_{0.8}Ni_{0.2}O_\delta$ and $Mn_{0.6}Ni_{0.4}O_\delta$ capacitors decrease to 190, 276, and 176 F g^{-1}, respectively. When increasing discharging current density from 0.155 to 1.24 A g^{-1}, the SC values for the symmetrical MnO_δ, $Mn_{0.8}Ni_{0.2}O_\delta$ and $Mn_{0.6}Ni_{0.4}O_\delta$ capacitors decrease by 39%, 32%, and 46%, respectively, demonstrating the higher power property of the $Mn_{0.8}Ni_{0.2}O_\delta$ material. This is in agreement with the cyclic voltammetry result in Fig. 5(ii—b), where current response increases almost linearly with increasing scan rate.

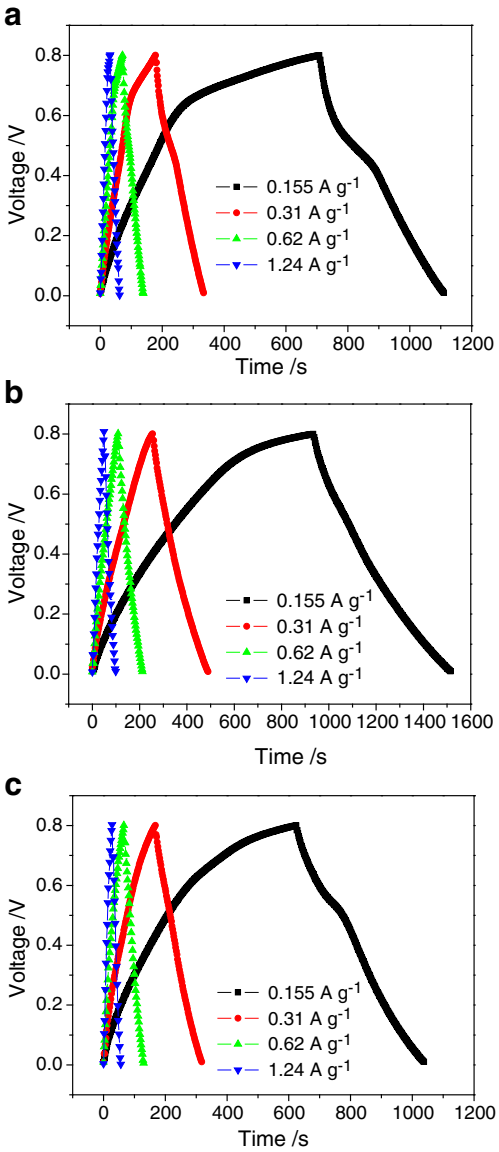

Fig. 6 Galvanostatic charge–discharge profiles of the symmetrical Mn–Ni oxide capacitors of (**a**) MnO_δ, (**b**) $Mn_{0.8}Ni_{0.2}O_\delta$, and (**c**) $Mn_{0.6}Ni_{0.4}O_\delta$ at various current densities, using an aqueous solution of 6 mol L^{-1} KOH as the electrolyte

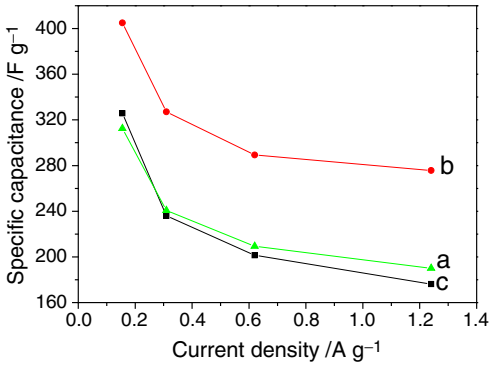

Fig. 7 Current density dependence of SC values of the symmetrical capacitors of (**a**) MnO_δ, (**b**) $Mn_{0.8}Ni_{0.2}O_\delta$, and (**c**) $Mn_{0.6}Ni_{0.4}O_\delta$, using an aqueous solution of 6 mol L^{-1} KOH as the electrolyte

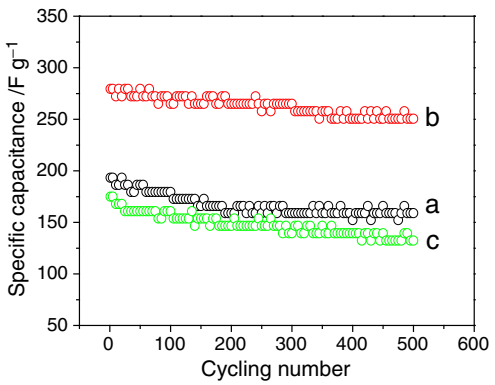

Fig. 8 Cycling life of the symmetrical Mn–Ni oxide capacitors of (**a**) MnO_δ, (**b**) $Mn_{0.8}Ni_{0.2}O_\delta$, and (**c**) $Mn_{0.6}Ni_{0.4}O_\delta$ at a current density of 1.24 A g^{-1} between 0 and 0.8 V, using an aqueous solution of 6 mol L^{-1} KOH as the electrolyte

To evaluate the long-term cycling stability of the obtained Mn–Ni oxide materials, the symmetrical capacitors were subjected to charge/discharge cycling at a current density of 1.24 A g^{-1} for consecutive 500 cycles. The variation of SC values of the symmetrical capacitors with cycle number is shown in Fig. 8. For the symmetrical MnO_δ capacitor, its SC fades fast during the first 146 cycles, then decreases slightly and becomes stable during the next 354 cycles. After 500 cycles, the symmetrical MnO_δ capacitor presents a SC value of 160 F g^{-1}, retaining ~82% of its initial SC. For the symmetrical $Mn_{0.8}Ni_{0.2}O_\delta$ capacitor, its SC fades slowly during the first 360 cycles, followed by getting stable during the next 140 cycles. After 500 cycles, the symmetrical $Mn_{0.8}Ni_{0.2}O_\delta$ capacitor exhibits a considerable SC value of 250 Fg^{-1}, retaining ~89% of its initial SC. As for the symmetrical $Mn_{0.6}Ni_{0.4}O_\delta$ capacitors, its SC fades almost continuously without a stable SC value approached during 500 cycles. Subjected to 500 cycles, the symmetrical $Mn_{0.6}Ni_{0.4}O_\delta$ capacitor possesses a SC value of 132 F g^{-1}, remaining 75% of its initial SC. Therefore, compared with the MnO_δ and $Mn_{0.6}Ni_{0.4}O_\delta$ materials, the $Mn_{0.8}Ni_{0.2}O_\delta$ material shows not only larger SC but also higher cycling stability, which is of practical importance.

Conclusions

Mesoporous Mn–Ni oxides with the chemical compositions of $Mn_{1-x}Ni_xO_\delta$ (x=0, 0.2, and 0.4) were prepared by a solid-state reaction route. The Mn–Ni oxides mainly consist of the α- and γ-MnO_2 phases, whose crystallinity appreciably decreases with increasing the Ni content. The SC values for the MnO_δ, $Mn_{0.8}Ni_{0.2}O_\delta$ and $Mn_{0.6}Ni_{0.4}O_\delta$ were 343, 528, and 411 F g^{-1} at a scan rate of 2 mV s^{-1}, and decreased to 157, 183, and 130 F g^{-1} with increasing scan rate to 100 mV s^{-1}, respectively. Subjected to 500 cycles at a current density of 1.24 A g^{-1}, the symmetrical MnO_δ, $Mn_{0.8}Ni_{0.2}O_\delta$ and $Mn_{0.6}Ni_{0.4}O_\delta$ capacitors deliver the SC of 160, 250, and 132 F g^{-1}, respectively, retaining about 82%, 89%, and 75% of their respective initial SC. Incorporation of a proper amount of nickel into the pristine manganese oxide notably improves its capacitive performance. In comparison with the MnO_δ and $Mn_{0.6}Ni_{0.4}O_\delta$, the $Mn_{0.8}Ni_{0.2}O_\delta$ shows larger SC, higher power property and good cycling stability. The prepared $Mn_{0.8}Ni_{0.2}O_\delta$ material has been demonstrated to be a promising candidate for supercapacitor materials.

Acknowledgements This work is financially supported by the Natural Science Foundation of Education Commission of Anhui Province under Grant nos. KJ2008A003 and KJ2009B050. The financial support provided by the Innovation Project of Anhui University of Technology and the Foundation of Young Teachers of Anhui University of Technology (Grant no.QZ200804) is gratefully acknowledged.

References

1. Conway BE (1999) Electrochemical Supercapacitors. Kluwer, New York
2. Burke A (2000) J Power Sources 91:37–50
3. Miller JR, Burke A (2008) Electrochem Soc Interface 17:53–57
4. Portet C, Taberna PL, Simon P, Flahaut E, Laberty RC (2005) Electrochim Acta 50:4174–4181
5. Simon P, Burke A (2008) Electrochem Soc Interface 17:38–43
6. Nathan T, Aziz A, Noor AF, Prabaharan SRS (2008) J Solid State Electrochem 12:1003–1009
7. Prasad KR, Miura N (2004) Electrochem Commun 6:1004–1008
8. Cheng J, Cao GP, Yang YS (2006) J Power Sources 159:734–741
9. Bélanger D, Brousse T, Long JW (2008) Electrochem Soc Interface 17:49–52
10. Sun LJ, Liu XX, Lau KKT, Chen L, Gu WM (2008) Electrochim Acta 53:3036–3042
11. Guan H, Fan LZ, Zhang HC, Qu XH (2010) Electrochim Acta 56:964–968
12. Zheng JP, Jow TR (1999) Electrochem Solid-State Lett 2:359–361
13. Lee HY, Goodenough JB (1999) J Solid State Chem 144:220–223
14. Reddy RN, Reddy RG (2004) J Power Sources 132:315–320
15. Zhang FB, Zhou YK, Li HL (2004) J Mater Chem Phys 83:260–264
16. Liu XM, Zhang XG, Fu SY (2006) Mater Res Bull 41:620–627
17. Wei TY, Chen CH, Chang KH, Lu SY, Hu CC (2009) Chem Mater 21:3228–3233
18. Gao YY, Chen SL, Cao DX, Wang GL, Yin JL (2010) J Power Sources 195:1757–1760
19. Brousse T, Toupin M, Dugas R, Athouël L, Crosnier O, Bélange D (2006) J Electrochem Soc 153:A2171–A2180
20. Athouel L, Moser F, Dugas R, Crosnier O, Bélanger D, Brousse T (2008) J Phys Chem C 112:7270–7277
21. Liu EH, Li W, Li J, Meng XY, Tan ST (2009) Mater Res Bull 44:1122–1126
22. Nakayama M, Tanaka A, Sato Y, Tonosaki T, Ogura K (2005) Langmuir 21:5907–5913
23. Xie XY, Liu WW, Zhao LY, Huang CD (2010) J Solid State Electrochem 14:1585–1594
24. Kim H, Popov BN (2003) J Electrochem Soc 150:D56–D62
25. Zhao GY, Xu CL, Li HL (2007) J Power Sources 163:1132–1136
26. Machefaux E, Brousse T, Bélanger D, Guyomard D (2007) J Power Sources 165:651–655
27. Wu MS, Huang YA, Yang CH (2008) J Electrochem Soc 155: A798–A805
28. Wang YG, Xia YY (2006) Electrochimica Acta 51:3223–3227
29. Fang DL, Wang ZB, Yang PH, Liu W, Chen CS (2006) J Am Ceram Soc 89:230–235
30. Fang DL, Wu BC, Mao AQ, Yan Y, Zheng CH (2010) J Alloy Comp 507:526–530
31. Rouquerol F, Rouquerol J, Sing K (1999) Adsorption by Powers and Porous Solids: Principles Methodology and Applications. Academic, San Diego
32. Sreethawong T, Chavadej S, Ngamsinlapasathian S, Yoshikawa S (2007) Colloids Surf A 296:222–229
33. Li J, Wang XY, Huang QH, Gamboa S, Sebastian PJ (2006) J Power Sources 160:1501–1505
34. Rogulski Z, Siwek H, Paleska I, Czerwinski A (2003) J Electroanal Chem 543:175–185
35. Hu CC, Tsou TW (2003) J Power Sources 115:179–186
36. Toupin M, Brousse T, Bélanger D (2002) Chem Mater 14:3946–3952
37. Bao SJ, He BL, Liang YY, Zhou WJ, Li HL (2005) Mater Sci Eng A 39:305–309